Translational and Rotational Damping of Flapping Flight and Its Dynamics and Stability at Hovering

Bo Cheng and Xinyan Deng

***Abstract*—Body movements of flying insects change their effective wing kinematics and, therefore, influence aerodynamic force and torque production. It was found that substantial aerodynamic damping is produced by flapping wings through a passive mechanism termed "flapping countertorque" during fast yaw turns. We expand this study to include the aerodynamic damping that is produced by flapping wings during body translations and rotations with respect to all its six principal axes—roll, pitch, yaw, forward/backward, sideways, and heave. Analytical models were derived by the use of a quasi-steady aerodynamic model and blade-element analysis by the incorporation of the effective changes of wing kinematics that are caused by body motion. We found that aerodynamic damping, in all these cases, is linearly dependent on the body translational and angular velocities and increases with wing-stroke amplitude and frequency. Based on these analytical models, we calculated the stability derivatives that are associated with the linearized flight dynamics at hover and derived a complete 6-degree-of-freedom (6-DOF) dynamic model. The model was then used to estimate the flight dynamics and stability of four different species of flying insects as case studies. The analytical model that is developed in this paper is important to study the flight dynamics and passive stability of flying animals, as well as to develop flapping-wing micro air vehicles (MAVs) with stable and maneuverable flight, which is achieved through passive dynamic stability and active flight control.**

***Index Terms*—Biologically inspired robots, biomimetics, dynamics, flapping wing, flight stability.**

I. Introduction

FLAPPING-WING insects fly with unprecedented maneuverability and stability compared with conventional aircraft [1], [2]. In comparison with fixed and rotary wing aircraft, flapping-wing fliers take advantage of more complicated aerodynamic mechanisms in low-speed flows [3], which have been well studied in recent years by the usage of experimental (e.g., [4]–[10]) or computational (e.g., [11]–[13]) techniques. On the other hand, high-speed videography (e.g., [2], [14]) provides detailed observations of insect flight kinematics and helps us to understand flight dynamics and control. However, the observed free-flight behavior can offer only a "closed-loop" view of overall flight dynamics, which has resulted from a complex synthesis of sensing, control, and actuation systems. Therefore, it is desirable to have an understanding of "open-loop" flight dynamics.

Through the use of computational fluid dynamics methods [15], [16], most previous studies showed that insect flight is inherently unstable and that the active modulation of wing kinematics might be the key to achieve the observed maneuverability and stability [2], [17]. However, recent studies on the turning dynamics of animal flight [18], [19] showed that during low-speed yaw turns, flapping-wing fliers that range in size from fruit flies to large birds are subject to substantial passive damping through an aerodynamic mechanism termed "flapping countertorque" (FCT). FCT is generated as a result of the asymmetries of wing motion that are induced by body yaw angular velocity during saccades. As an inherent property, FCT helps the flapping-wing fliers to slow down body rotation during rapid maneuvers, thus, reducing the required active torque that is produced by the asymmetries of wing motion. As a tradeoff, however, flapping-wing fliers must overcome extensive aerodynamic damping to accelerate or to initiate a maneuver [18].

Not only body yaw rotation, but body movement as well, in general, will induce counterforce/countertorque that acts against it. For example, simulation results [18] have shown that substantial aerodynamic damping exists also for body roll and pitch rotations. It was also found that in forward flight, relative airspeed will induce a drag that is opposite from the flight direction that varies linearly with airspeed [20]. Buelthoff *et al.* [21] showed that the turning rate of a saccade is inversely related to the forward velocity, which might reflect an aerodynamic constraint on the flight dynamics. Therefore, a comprehensive understanding of how body translations and rotations influence the aerodynamic force/torque production is crucial for further exploration of flapping-wing flight dynamics.

This paper is organized as follows. In Section II, by the investigation of the geometric changes of wing motion that are caused by different types of body movements (translations along and rotations about the principal axes of the body frame), we derive analytical models to estimate the aerodynamic damping that is produced during maneuvers along each principle axis. In Section III, based on these analytical models, we calculate the stability derivatives that are associated with flight dynamics at hover. A complete mathematical model of 6-degree-of-freedom (6-DOF) flight dynamics is then provided. The predictions by the derived analytical models are compared with the existing experimental and computational results. The effects of unsteady aerodynamic mechanisms and other modeling issues are then discussed in Section IV. Finally, in Section V, conclusions and

Manuscript received April 7, 2011; accepted May 9, 2011. Date of publication June 16, 2011; date of current version October 6, 2011. This paper was recommended for publication by Associate Editor Y. Sun and Editor J.-P. Laumond upon evaluation of the reviewers' comments. The work was supported by National Science Foundation CAREER IIS under Award 0545931.

The authors are with School of Mechanical Engineering, Purdue University, West Lafayette, IN 47907, USA (e-mail: bcheng@purdue.edu; xdeng@purdue.edu).

Color versions of one or more of the figures in this paper are available online at http://ieeexplore.ieee.org.

Digital Object Identifier 10.1109/TRO.2011.2156170

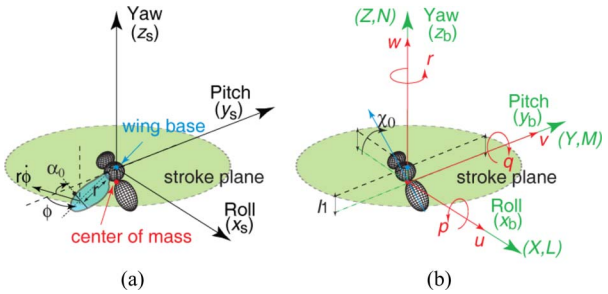

Fig. 1. Schematic view of coordinate systems and kinematics. (a) Stroke plane frame coordinates that originated from wing base (blue dot). Wing kinematics are specified by the stroke angle ϕ and the (geometric) angle of attack α_0, which is defined as the angle between the wing chord and the tangential of the wing's trajectory (relative to the stroke plane). (b) Body coordinate frame has the same orientation as the stroke plane frame but with the origin that is located at the center of mass (red dot). Body kinematics are specified by the translational velocity (u, v, w) along and angular (p, q, r) velocity about three principal axes of the body frame. The total forces (X, Y, Z) and torques (L, M, N) that are produced by the wing pair are also shown. Note that the wing velocity $r\dot{\phi}$ is positive during upstroke and negative during downstroke, according to the definition of the stroke angle.

future research directions are presented. Detailed mathematical derivations are presented in Appendix A, and we present the experimental results by the use of four different species of insect flight data in Appendix B.

II. Theoretical Estimations of Aerodynamic Damping

In this section, we will derive analytical models to estimate the aerodynamic damping that acts against the body movement of flapping-wing fliers. The aerodynamic forces are calculated by the use of quasi-steady aerodynamic models [6], [10] and blade-element analysis. We consider one pair of wings with symmetrical kinematics relative to the body. The body motion changes the effective wing kinematics (relative to the global frame) and, therefore, affects the aerodynamic force and torque produced. Geometrically, the body motion changes the wing kinematics in the following three ways:

1) effective angle of attack;
2) chordwise wing velocity;
3) spanwise wing velocity.

We are able to incorporate these changes into force/torque production by the use of blade-element analysis. In this section, the analytical models are derived by the assumption that the angle of attack is the major parameter that determines force coefficients. The effects of other kinematic parameters and of neglected aerodynamic mechanisms are discussed in Section IV with necessary modifications to the model that we derived.

The coordinate systems and conventions of body and wing kinematics that are used in this study are shown in Fig. 1. Note that in this study, we construct the body frame and the stroke plane frame with the same orientation; therefore, translational velocity components in the body frame (u, v, w) are equivalent to those in the stroke plane frame (v_{xs}, v_{ys}, v_{zs}). In Section II-A–E, we derive the models of aerodynamic damping with respect to body translations along and rotations about three principal axes of the stroke plane frame [see Fig. 1(a)].

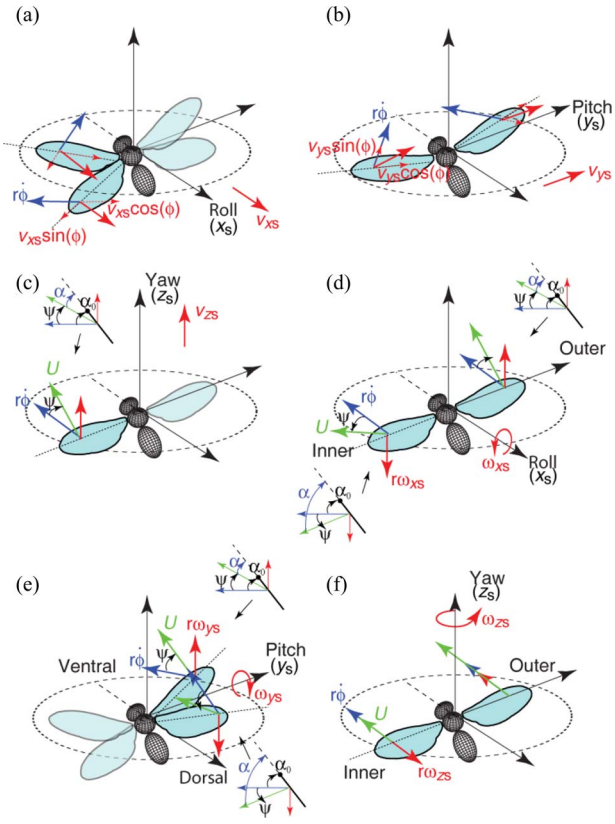

Fig. 2. Schematic view of wing kinematic parameters during translations and rotations of the stroke plane. The total sectional wing velocity (U, green arrows) is composed of wing flapping $r\dot{\phi}$ (blue arrows) and body-motion-induced velocity (red arrows). ψ represents the directional change of the sectional velocity, and α and α_0 are the effective and geometric angles of attack, respectively. (a) Moving backward. (b) Moving to the right. (c) Vertical ascent. (d) Roll rotation. (e) Pitch rotation. (f) Yaw rotation.

A. During Forward/Backward Translation

Forward/backward body translation along the roll axis x_s of the stroke plane [see Fig. 2(a)] changes both the direction and the magnitude of local wing velocity without affecting the geometric angle of attack. It adds or subtracts the chordwise wing velocity by $v_{xs}\cos(\phi)$ and the spanwise velocity by $v_{xs}|\sin(\phi)|$ [see Fig. 2(a)]. Before we proceed, we will first define two nondimensional parameters that will prove useful in our analysis. The chordwise tip velocity ratio [22] is defined as

$$\mu_x = \frac{v_{xs}\cos(\phi)}{R(d\phi/dt)} \tag{1}$$

where the subscript x indicates that the translation is along the roll axis, and V_{xs} is the velocity. μ describes the ratio of the chordwise wing-tip velocity that results from body translations and wing flapping. A positive value indicates an enhancement of the chordwise velocity. Similarly, the spanwise tip velocity ratio is defined as

$$\gamma_x = -\frac{v_{xs}\sin(\phi)}{R(|d\phi/dt|)}. \tag{2}$$

It describes the ratio of the spanwise velocity (resulting from body translation) and the chordwise velocity (resulting from

wing flapping). A positive value corresponds to a spanwise flow from wing base to tip. Through standard blade-element analysis, Dickson and Dickinson [22] give the aerodynamic force that acts on a wing as

$$F(\hat{t}) = \frac{1}{8}\rho R^3 \bar{c}\Phi^2 n^2 C_F(\alpha)\left(\frac{d\hat{\Phi}}{d\hat{t}}\right)^2 \left(\hat{r}_2^2(S) + 2\hat{r}_1^1(S)\mu_x + \mu_x^2\right) \quad (3)$$

at nondimensional time $\hat{t}$ ($\hat{t} = tn$), where F is the magnitude of a specific force component (lift, drag, and normal force), $C_F(\alpha)$ is the corresponding force coefficient, α is the effective angle of attack (we denote the geometric angle of attack as α_0), $d\hat{\phi}/d\hat{t}$ is the nondimensional flapping velocity of the wing, Φ and n are, respectively, the wing-flapping amplitude and frequency, and $\hat{r}_1^1(S)$ and $\hat{r}_2^2(S)$ are, respectively, the nondimensional first and second moments of the wing area.

Next, we calculate the total aerodynamic force that acts on the wings by the careful investigation of the changes of the angle of attack and wing velocity that are induced by body movement (see Appendix A). We find that the stroke-averaged lift is unaltered by forward/backward translations (by ignoring higher order terms). However, there exists a stroke-averaged drag that acts opposite to the direction of translation, which is given by

$$\bar{X} = -\rho R^2 \bar{c}\Phi n \hat{r}_1^1(S)\overline{C_D(\alpha_0)\cos^2(\phi)\left|\frac{d\hat{\phi}}{d\hat{t}}\right|}u. \quad (4)$$

We termed it "flapping counterforce" (FCF). Meanwhile, the net drag force (4) induces a pitch moment around the center of mass with a moment arm l_1 (i.e., the distance between the wing base and the center of mass), and we can find a stroke-averaged pitch torque that is given by

$$\bar{M} = -\rho R^2 \bar{c}\Phi n \hat{r}_1^1(S) l_1 \overline{C_D(\alpha_0)\cos^2(\phi)\left|\frac{d\hat{\phi}}{d\hat{t}}\right|}u. \quad (5)$$

B. During Lateral Translation

Similar to forward/backward translation, lateral body translation along the pitch axis y_s of the stroke plane [see Fig. 2(b)] changes both the direction and the magnitude of local wing velocity without changing the geometric angle of attack. It adds or subtracts the chordwise wing velocity by $v_{ys}|\sin(\phi)|$ and the spanwise velocity by $v_{ys}\cos(\phi)$. The chordwise and spanwise tip velocity ratios, here, are given, respectively, by

$$\mu_y = \frac{v_{ys}\sin(\phi)}{R(d\phi/dt)} \quad (6)$$

and

$$\gamma_y = (-1)^i \frac{v_{ys}\cos(\phi)}{R(|d\phi/dt|)} \quad (7)$$

where the subscript y indicates that the translation is along the pitch axis, v_{ys} is the velocity, and i equals 0 for the left wing and 1 for the right wing.

We can see that during lateral translation to the right [see Fig. 2(b)], the spanwise flow is always from wing base to tip for the left wing (positive γ_y) and from tip to base for the right wing (negative γ_y). μ_y is positive when the wing flaps to the right [e.g., the left wing's second half of downstroke, as shown in Fig. 2(b)], and negative when it flaps to the left. By the consideration of the changes of body translation on the total force production (see Appendix A), we can collectively show that the stroke-averaged force (FCF) is acting opposite to the direction of lateral translation and is given by

$$\bar{Y} = -\rho R^2 \bar{c}\Phi n \hat{r}_1^1(S)\overline{C_D(\alpha_0)\sin^2(\phi)\left|\frac{d\hat{\phi}}{d\hat{t}}\right|}v. \quad (8)$$

A roll torque is also produced about the center of mass, and its stroke-averaged value can be calculated by

$$\bar{L} = \rho R^2 \bar{c}\Phi n \hat{r}_1^1(S) l_1 \overline{C_D(\alpha_0)\sin^2(\phi)\left|\frac{d\hat{\phi}}{d\hat{t}}\right|}v. \quad (9)$$

C. During Vertical Translation

As shown in Fig. 2(c), the translational velocity along the vertical axis z_s changes the direction of flapping velocity at a wing section by

$$\psi = \arctan\left(\frac{v_{zs}}{r|d\phi/dt|}\right) \quad (10)$$

where r is the spanwise position of wing section, and v_{zs} is the translational velocity along the z_s axis. Therefore, the effective angle of attack is modified by ψ. (Positive ψ corresponds to a reduction of angle of attack.) The magnitude of the total wing velocity at a wing section is

$$U = \frac{r|d\phi/dt|}{\cos(\psi)} = \sqrt{\left(r\frac{d\phi}{dt}\right)^2 + v_{zs}^2}. \quad (11)$$

Next, if we approximate the normal force coefficient by

$$C_N(\alpha_0+\psi) \approx C_N(\alpha_0) + \frac{dC_N(\alpha)}{d\alpha}_{|\alpha=\alpha_0}\psi \approx C_N(\alpha_0) + \frac{dC_N(\alpha)}{d\alpha}_{|\alpha=\alpha_0}\left(\frac{v_{zs}}{r|d\phi/dt|}\right) \quad (12)$$

and then apply the blade-element theory, we have the net lift change of a wing pair (see Appendix A):

$$Z(t) = -\frac{1}{2}\rho R^2 \bar{c}\Phi n\left|\frac{d\hat{\phi}}{d\hat{t}}\right|\cos(\alpha_0)\frac{dC_N(\alpha)}{d\alpha}_{|\alpha=\alpha_0}\hat{r}_1^1(S)w \quad (13)$$

at nondimensional time $\hat{t}$. The stroke-averaged value is

$$\bar{Z} = -\frac{1}{2}\rho R^2 \bar{c}\hat{r}_1^1(S)\Phi n\overline{\frac{dC_N(\alpha)}{d\alpha}_{|\alpha=\alpha_0}\cos(\alpha_0)\left|\frac{d\hat{\phi}}{d\hat{t}}\right|}w \quad (14)$$

that acts opposite from the direction of translation.

D. During Roll Rotation

During a roll rotation [e.g., see Fig. 2(d)], the effective angle of attack α of the inner wing (left wing in this figure) is increased (or lowered) when the one of the outer wing is lowered (or increased). The change of the angle of attack is identical at all wing sections and is given by

$$\psi = (-1)^i \arctan\left(\frac{\omega_{xs}\cos(\phi)}{|d\phi/dt|}\right) \approx (-1)^i \left(\frac{\omega_{xs}\cos(\phi)}{|d\phi/dt|}\right) \tag{15}$$

where *i* equals 1 for the inner wing and 0 for the outer wing, and ω_{xs} is the angular velocity about the roll axis of the stroke plane. The total wing velocity at a wing section is

$$U = \frac{r|d\phi/dt|}{\cos(\psi)} = r\sqrt{\left(\frac{d\phi}{dt}\right)^2 + \omega_{xs}^2}. \tag{16}$$

More specifically, the angular velocity about the roll axis induces a downward velocity at the left half of the stroke plane, thereby, increasing the inner (left) wing's angle of attack. Similarly, it induces an upward velocity at the right half of the stroke plane and reduces the angle of attack of the outer (right) wing. Therefore, the inner wing is expected to produce a larger magnitude of force than the outer wing. If we approximate the force coefficient as in (12), through the blade-element analysis, the net roll torque around the center of mass is

$$L(\hat{t}) \approx -\frac{1}{2}\rho R^4 \bar{c}\hat{r}_3^3(S)\frac{dC_N(\alpha)}{d\alpha}_{|\alpha_0}\cos(\alpha_0)\cos^2(\phi)\left|\frac{d\hat{\phi}}{d\hat{t}}\right|\Phi n \tag{17}$$

at nondimensional time $\hat{t}$, where $\hat{r}_3^3(S)$ is the nondimensional third moment of the wing area. Note that, during a roll (or pitch) rotation around the center of mass, there will be a small amount of the translational velocity of the stroke plane (because of the distance between the wing base and the center of mass), which is neglected here (see Section IV). The averaged value over one wing stroke is

$$\bar{L} \approx -\frac{1}{2}\rho R^4 \bar{c}\hat{r}_3^3(S)\overline{\frac{dC_N(\alpha)}{d\alpha}_{|\alpha_0}\cos(\alpha_0)\cos^2(\phi)\left|\frac{d\hat{\phi}}{d\hat{t}}\right|}\Phi np \tag{18}$$

which is a restoring torque (FCT) that acts opposite from the direction of rotation.

E. During Pitch Rotation

During a pitch rotation [e.g., see Fig. 2(e)], the pitch angular velocity induces an upward velocity at the ventral (anterior) half of the stroke plane and reduces the effective angle of attack α during the ventral-to-middle and middle-to-ventral strokes. Similarly, it induces a downward velocity at the dorsal (posterior) half of the stroke plane and increases the effective angle of attack during the dorsal-to-middle and middle-to-dorsal strokes. The change of the angle of attack is identical at all wing sections and is given by

$$\psi \approx \arctan\left(\frac{\omega_{ys}\sin(\phi)}{|d\phi/dt|}\right) \approx \left(\frac{\omega_{ys}\sin(\phi)}{|d\phi/dt|}\right) \tag{19}$$

where ω_{ys} is the angular velocity about the pitch axis of the stroke plane. The magnitude of the total wing velocity at a wing section (*r*) is

$$U = \frac{r|d\phi/dt|}{\cos(\psi)} = r\sqrt{\left(\frac{d\phi}{dt}\right)^2 + \omega_{ys}^2}. \tag{20}$$

Again, by the application of the blade-element model (see Appendix A), we can find a stroke-averaged restoring torque (FCT) that acts in the opposite direction of pitch rotation

$$\bar{M} \approx -\frac{1}{2}\rho R^4 \bar{c}\hat{r}_3^3(S)\overline{\frac{dC_N(\alpha)}{d\alpha}_{|\alpha_0}\cos(\alpha_0)\sin^2(\phi)\left|\frac{d\hat{\phi}}{d\hat{t}}\right|}\Phi nq. \tag{21}$$

F. During Yaw Rotation

The aerodynamic damping during yaw rotation is well described in the previous studies [18], [19], [23]. The instantaneous resorting yaw torque (FCT) and its stroke-averaged value are given by

$$N(\hat{t}) = -\rho R^4 \bar{c}\hat{r}_3^3(S)\Phi C_D(\alpha_0)\left|\frac{d\hat{\phi}}{d\hat{t}}\right| nr \tag{22}$$

$$\bar{N} = -\rho R^4 \bar{c}\hat{r}_3^3(S)\overline{\Phi C_D(\alpha_0)\left|\frac{d\hat{\phi}}{d\hat{t}}\right|} nr \tag{23}$$

where ω_{zs} is the yaw angular velocity in the stroke plane frame.

Our calculation indicates that for each type of rotation, the stroke-averaged FCT acts strictly opposite to the directions of rotation (collinear with the rotation axis). In other words, there is no resultant torque about any axis that is perpendicular to the rotation axis, and this is consistent with previous simulation results [18]. Note that although the stroke plane frame and the body frame are originated from different positions (see Fig. 1), the moment arms about the principal axes are identical in the calculations made earlier (see Appendix A); therefore, FCTs are expressed directly in the body coordinate frame.

III. Stability Derivatives and Linearized Flight Dynamics During Hover

A detailed description of linearized flight dynamics can be found in [24] and [25]. See [26] for related studies about linearized hovering flight dynamics. An analytical investigation is given in the present context that is based on the mathematical models of stroke-averaged FCT and FCF. We first consider the insect body that is oriented with a fixed pitch angle χ_0 (free body angle) relative to the horizontal stroke plane (see Fig. 1). As previously introduced, the stroke plane frame (x_s, y_s, z_s) is fixed relative to the body with the origin that is located at the wing base (see Fig. 1). We defined the body frame (x_b, y_b, z_b) having the same orientation with the stroke plane frame but with the origin that is located at the center of mass (see Fig. 1). The distance between the wing base and the center of mass is specified by l_1. If the insect body is modeled as a rigid

body, its complete dynamics are described by the Newton–Euler equations of motion [27], which comprise six equations with translational velocity (u, v, w) and angular velocity (p, q, r) as unknowns. With the addition of another six kinematic equations that describes the body position (x, y, z) and orientation (ϕ_b, θ_b, ψ_b) (the subscripts are used to differentiate the angles that are used in body and wing kinematics) relative to the Earth-fixed frame, a complete system of equations includes 12 coupled nonlinear ordinary differential equations that incorporate the aerodynamic forces (x, y, z) and torques (L, M, N), acting along or around the body axes. Because the body position (x, y, z) and heading angle ψ_b do not affect the aerodynamic steady state, they can be considered separately with appropriate equations [24]. Therefore, the following autonomous system of equations can be extracted from the full system (12 kinematic and dynamic equations of motion) to study the flight dynamics in the absence of control inputs:

$$\dot{u} = -(wq - vr) + \frac{X}{m} + g\ \sin\ \theta_b \tag{24a}$$

$$\dot{v} = -(ur - wp) + \frac{Y}{m} - g\cos\theta_b \sin\phi_b \tag{24b}$$

$$\dot{w} = -(vp - uq) + \frac{Z}{m} - g\cos\theta_b \cos\phi_b \tag{24c}$$

$$I_{xx}\dot{p} - I_{xz}\dot{r} = (I_{yy} - I_{zz})qr + I_{xz}pq + L \tag{24d}$$

$$I_{yy}\dot{q} = (I_{zz} - I_{xx})pr + I_{xz}(r^2 - p^2) + M \tag{24e}$$

$$I_{zz}\dot{r} - I_{xz}\dot{p} = (I_{xx} - I_{yy})pq - I_{xz}qr + N \tag{24f}$$

$$\dot{\phi}_b = p + q\ \sin\phi_b \tan\theta_b + r\ \cos\ \phi_b \tan\theta_b \tag{24g}$$

$$\dot{\theta}_b = q\ \cos\ \phi_b - r\phi_b \tag{24h}$$

where the state vector x is equal to $(u, w, q, \theta_b, v, p, r, \phi_b)^T \in R^8$; m is the body mass; I_{xx}, I_{yy}, and I_{zz} are the moments of inertia about the body axes (x_b, y_b, z_b); and I_{xz} is the product of inertia (I_{yz} and I_{xy} are zero, since the xz plane is a plane of symmetry).

To analyze the near-hover flight dynamics, we can linearize the equations of motion by the use of small perturbation theory. A crucial step in the linearization process is to approximate the aerodynamic forces and torques as the analytical functions of the perturbed motion variables (i.e., stability derivatives multiplied by the corresponding disturbance quantity of the motion variables), as well as to obtain the stability derivatives. A complete description of this method can be found in [24]. Because the aerodynamics are mainly affected by velocities, we consider only the first derivatives with respect to time (e.g., X_u) and neglect the effects of the second derivatives (e.g., $X_{\dot{u}}$) and other nonlinear terms (see Section IV), which is justified in most flight conditions [24], [28].

In the previous studies of longitudinal dynamics, Taylor and Thomas [25] measured the stability derivatives from the tethered desert locust *Schistocerca gregaria* in an open-circuit low-speed wind tunnel; alternatively, Sun and coworkers used computational fluid dynamics to calculate stability derivatives in hovering insect models [15], [16]. In this study, because we have already obtained the analytical estimations of aerodynamic damping during body translations and rotations (FCTs and FCFs), we are able to derive the estimations of stability derivatives by the use of those models. Table I summarizes the nondimensional forms of stability derivatives with nonzero values. Notably, the axis x_s (y_s) does not coincide with the axis x_b (y_b) (see Fig. 1); therefore, a rotation around x_b (y_b) corresponds to a rotation around x_s (y_s) plus a linear translation of the stroke plane. We neglected the effect of this translation for simplification (see Section IV).

TABLE I
ANALYTICAL ESTIMATIONS OF NONDIMENSIONAL STABILITY DERIVATIVES WITH NONZERO VALUES

Non-dimensional Stability derivatives	Analytical estimations
X_u^+	$-\frac{\hat{r}_1^1(S)}{2\hat{r}_2(S)}\overline{C_D(\alpha_0)\cos^2(\phi)\lvert d\hat{\phi}/d\hat{t}\rvert}$
Y_v^+	$-\frac{\hat{r}_1^1(S)}{2\hat{r}_2(S)}\overline{C_D(\alpha_0)\sin^2(\phi)\lvert d\hat{\phi}/d\hat{t}\rvert}$
Z_w^+	$-\frac{\hat{r}_1^1(S)}{4\hat{r}_2}\overline{\frac{dC_N(\alpha)}{d\alpha}_{\lvert\alpha=\alpha_0}\cos(\alpha_0)\lvert d\hat{\phi}/d\hat{t}\rvert}$
L_p^+	$-\frac{AR}{16\Phi}\frac{\hat{r}_3^3}{\hat{r}_2^2}\overline{\frac{dC_N(\alpha)}{d\alpha}_{\lvert\alpha_0}\cos^2(\phi)\cos(\alpha_0)\lvert d\hat{\phi}/d\hat{t}\rvert}$
L_v^+	$\frac{\hat{r}_1^1(S)}{4\hat{r}_2(S)}AR\hat{l}_1\hat{L}\overline{C_D(\alpha_0)\sin^2(\phi)\lvert d\hat{\phi}/d\hat{t}\rvert}$
M_q^+	$-\frac{AR}{16\Phi}\frac{\hat{r}_3^3}{\hat{r}_2^2}\overline{\frac{dC_N(\alpha)}{d\alpha}_{\lvert\alpha_0}\sin^2(\phi)\cos(\alpha_0)\lvert d\hat{\phi}/d\hat{t}\rvert}$
M_u^+	$-\frac{\hat{r}_1^1(S)}{4\hat{r}_2(S)}AR\hat{l}_1\hat{L}\overline{C_D(\alpha_0)\cos^2(\phi)\lvert d\hat{\phi}/d\hat{t}\rvert}$
N_r^+	$-\frac{AR}{8\Phi}\frac{\hat{r}_3^3}{\hat{r}_2^2}\overline{C_D(\alpha)\lvert d\hat{\phi}/d\hat{t}\rvert}$

Stability derivatives X_u, Y_v, and Z_w are nondimensionalized by $\rho UR\bar{c}$; L_p, M_q, and N_r are nondimensionalized by $\rho U^2 R\bar{c}^2/n$; L_v and M_u are nondimensionalized by $\rho UR\bar{c}^2$. Here, U equals $2\Phi nR\hat{r}_2$. The superscript "+" denotes the nondimensional values, AR is the aspect ratio, and $\bar{L}$ denotes the body length as a fraction of the wing length, i.e., L/R.

We assume hovering reference conditions

$$p_e = q_e = r_e = u_e = v_e = w_e = \theta_{b\,e} = \phi_{b\,e} = 0 \tag{25}$$

and the reference values of the aerodynamic forces and moments are

$$X_e = Y_e = L_e = M_e = N_e = 0, \quad Z_e = \frac{g}{m}. \tag{26}$$

Finally, the linearized equations of motion in the matrix form are written as follows:

$$\dot{x} = Ax = \begin{bmatrix} \frac{X_u}{m} & 0 & 0 & q & 0 & 0 & 0 & 0 \\ 0 & \frac{Z_w}{m} & 0 & 0 & 0 & 0 & 0 & 0 \\ C_3 M_u & 0 & C_3 M_q & 0 & 0 & 0 & 0 & 0 \\ 0 & 0 & 1 & 0 & 0 & 0 & 0 & 0 \\ 0 & 0 & 0 & 0 & \frac{Y_v}{m} & 0 & 0 & -g \\ 0 & 0 & 0 & 0 & C_4 L_v & C_4 L_p & C_1 N_r & 0 \\ 0 & 0 & 0 & 0 & C_1 L_v & C_1 L_p & C_1 N_r & 0 \\ 0 & 0 & 0 & 0 & 0 & 1 & 0 & 0 \end{bmatrix} x \tag{27}$$

where $x = (\delta u, \delta w, \delta q, \delta\theta_b, \delta v, \delta p, \delta r, \delta\phi_b)^T$

$$C_1 = \frac{I_{xz}}{I_{xx} I_{zz} - I_{xz}^2}$$
$$C_2 = \frac{I_{xx}}{I_{xx} I_{zz} - I_{xz}^2}$$
$$C_3 = \frac{1}{I_{yy}}$$
$$C_4 = \frac{I_{zz}}{I_{xx} I_{zz} - I_{xz}^2} \tag{28}$$

are constants of body moments of inertia, and *A* is the system matrix of the linearized dynamics. Note that by choosing a reference-body frame with the same orientation as the stroke plane frame (see Fig. 1) and then using the estimations of stability derivatives (see Table I), we can decouple the hovering dynamics into longitudinal (described by $[u, w, q, \theta_b]^T$) and lateral (described by $[v, p, r, \phi_b]^T$) dynamics, as illustrated by the structure of the system matrix *A*.

With the system matrix *A* determined, the linearized flight dynamics during hover can be evaluated by looking at the corresponding eigenvalues and eigenvectors. Next, we evaluate the stability derivatives and calculate the system matrix, by the usage of real insect morphological and kinematic data (see Table II in Appendix B). We choose the data from four different species with dissimilar flight dynamics [19]: fruit fly (*Drosophila melanogaster*), hawkmoth (*Manduca sexta*), stalk-eyed fly (*Cyrtodiopsis dalmanni*), and bumblebee (*Bombus*).

By the usage of the analytical estimations given in Table I, nondimensional stability derivatives (with nonzero values) are calculated. The results are summarized in Table III in Appendix B. With the stability derivatives known, the system matrix *A* in (27) is calculated, and the eigenvalues and corresponding eigenvectors can then be obtained accordingly (see Tables IV and V in Appendix B).

Notably, all four types of insects that are investigated exhibit similar natural modes of motion during hover in terms of longitudinal and lateral dynamics. The longitudinal dynamics consist of a fast stable subsidence mode (mode 1), an unstable oscillatory mode (mode 2), and a slow stable subsidence mode (mode 3), which agree with the previous computational fluid dynamics (CFD) results [15]. The fast-subsidence mode corresponds to an in-phase coupling of δu and δq, which results in a pitch-down (-up) motion accompanied by a forward (backward) translation with decaying magnitudes. In this mode, the forward translation reduces the pitch-down motion as indicated by a negative X_u^+; in the meantime, FCF and FCT both act to reduce the initial disturbances, therefore, resulting in stable subsequent motions. The unstable oscillatory mode corresponds to a near out-of-phase coupling of δu^+ and δq^+ (the phase difference is greater than 120° for all four insects); thus, in the larger part of an oscillating cycle, the insects pitch up (or down), while moving forward (or backward). In this mode, an initial pitch-down velocity is enhanced by a backward translation, thus magnifying the initial disturbances and leading to the instability. The slow-subsidence mode (mode 3) corresponds to a damped ascending/descending motion as the FCF in the vertical direction acts to reduce velocity.

Similar to the longitudinal dynamics, the lateral dynamics consist of two subsidence modes with relative fast (mode 4) and slow (mode 6) convergences and an unstable oscillatory mode (mode 5). The fast-subsidence mode corresponds to a highly damped yaw rotation (the larger value of nondimensional eigenvalues means less wing-beat time to reduce the initial disturbance; see Table IV in Appendix B) with an out-of-phase coupling of δv and δp. The initial rolling disturbance is reduced by the roll torque that is generated by the out-of-phase lateral velocities (as indicated by a positive L_v^+) and results in a stable motion. The yaw rotation is out-of-phase with the roll rotation. The slow-subsidence mode has a similar out-of-phase coupling of δv and δp, but with less-damped yaw rotation, which is now in phase with the roll rotation. The unstable oscillatory mode has a near in-phase coupling of δv and δp (the phase difference is less than 51° for all four insects), where lateral translation acts to enhance the initial rolling and leads to an unstable subsequent motion.

Despite the similarities of flight dynamics between the four insects, we find that the hawk moth has relatively faster natural modes of motion compared with other insects (see Table IV in Appendix B) in terms of wing-beat time. Assuming a motion of the natural mode (mode 4), for example, the hawk moth is able to passively reduce 63% of its initial yaw velocity in less than one wing beat ($1/\lambda_4^+ \approx 0.95$), but the fruit fly needs about one and a half wing beats, and the bumblebee and stalk-eyed fly need about three. This is consistent with the measurements that are compiled on free-flying insects exhibiting low-speed yaw turns [19], which suggests that the large-winged hawk moth has a deceleration half-life of less than one wing beat.

Compared with the CFD results by Sun and coworkers [15], [16], our analytical model predicts similar natural modes of motion in longitudinal dynamics. In lateral dynamics, however, though both studies found a fast-subsidence mode, Zhang and Sun [16] found the slow-oscillatory mode to be stable (we found it unstable) and the slow-divergence mode to be unstable (we found it stable). This discrepancy reflects the differences of

stability derivatives that are calculated between these two studies. Therefore, it is important for us to investigate the effects of the neglected aerodynamic mechanisms in the FCT and FCF models, which are used to calculate the stability derivatives.

IV. Discussion

A. Effects of Chordwise and Spanwise Tip Velocity Ratios

As mentioned previously, body translations and rotations bring three types of geometric changes to wing kinematics; they are the angle of attack α, chordwise tip velocity ratio μ [defined by (1) and (6)], and spanwise tip velocity ratio γ [defined by (2) and (7)]. In Section II, analytical models were obtained by the assumption that spanwise and chordwise flows modify only the sectional wing velocities without changing force coefficients (which depend only on the angle of attack). This is an appropriate assumption when modeling FCT during body rotations because force coefficients are unaffected in these situations. However, as shown by Dickson and Dickinson [22], uniform chordwise velocities (because of body translation) across the wingspan change both lift and drag force coefficients; therefore, a revised quasi-steady aerodynamic model is required to include this effect in forward/backward body translations. Furthermore, a recent CFD study [16] showed that additional spanwise flow that is caused by body lateral translation increases the strength of leading edge vortex when the flow is from wing base to tip and decreases it when from tip to base. Therefore, the wing with base-to-tip spanwise flow generates larger force than the one with tip-to-base spanwise flow. Similar phenomenon is also found in authors' laboratory by the usage of robotic wing experiments of translating flapping wings (unpublished). For example, body lateral translation to the left leads to an increase (decrease) of force produced by right (left) wing. Although the specific reason for this phenomenon is still not well known, all of these studies suggest that the force production is strongly dependent on the spanwise flow, which might require consideration in the current analysis. Therefore, in the following, a tentative model is given, by the assumption that the force coefficients are dependent on μ and γ. First, we approximate force coefficients by the use of first-order Taylor expansion

$$C_F(\alpha,\mu,\gamma)\approx C_F(\alpha,0,0)+\frac{\partial C_F(\alpha,0,0)}{\partial\mu}\mu+\frac{\partial C_F(\alpha,0,0)}{\partial\gamma}\gamma \tag{29}$$

where $C_F(\alpha, 0, 0)$ are identical to $C_F(\alpha)$, which are those measured in [6], and $\partial C_F(\alpha,0,0)/\partial\mu$ and $\partial C_F(\alpha,0,0)/\partial\gamma$ represent the partial derivatives of force coefficients to μ and γ, respectively. By the use of (29), we can show that the FCF during body forward/backward translation can now be calculated by (see Appendix A)

$$\bar{X}=-\rho R^2\bar{c}\Phi n\left[\hat{r}_1^1(S)\overline{C_D(\alpha_0)\cos^2(\phi)\left|\frac{d\hat{\phi}}{d\hat{t}}\right|}+\frac{1}{2}\frac{\partial C_D}{\partial\mu_x}\overline{\cos^2(\phi)\left|\frac{d\hat{\phi}}{d\hat{t}}\right|}\hat{r}_2^2(S)\right]u. \tag{30}$$

Note that the additional term [compared with (4)] results from the change of the drag force coefficient because of μ_x. In the meantime, the pitch torque around the center of mass (when moving forward/backward) is

$$\bar{M}=\rho R^2\bar{c}\Phi n\left[\frac{1}{2}\frac{\partial C_L}{\partial\gamma_x}\overline{\sin^2(\phi)\left|\frac{d\hat{\phi}}{d\hat{t}}\right|}\hat{r}_3^3(S)R-\hat{r}_1^1(S)l_1\overline{C_D(\alpha_0)\cos^2(\phi)\left|\frac{d\hat{\phi}}{d\hat{t}}\right|}-\frac{1}{2}l_1\frac{\partial C_D}{\partial\mu_x}\overline{\cos^2(\phi)\left|\frac{d\hat{\phi}}{d\hat{t}}\right|}\hat{r}_2^2(S)\right]u \tag{31}$$

where the first term in the parentheses results from the change of the lift force coefficient because of γ_x; the second and third terms represent the pitch moment induced by the drag (FCT) with a moment arm l_1. Similarly, we can show that during lateral translation

$$\bar{Y}=-\rho R^2\bar{c}\Phi n\left[\hat{r}_1^1(S)\overline{C_D(\alpha_0)\sin^2(\phi)\left|\frac{d\hat{\phi}}{d\hat{t}}\right|}+\frac{1}{2}\frac{\partial C_D}{\partial\mu_y}\overline{\sin^2(\phi)\left|\frac{d\hat{\phi}}{d\hat{t}}\right|}\hat{r}_2^2(S)\right]v \tag{32}$$

and

$$\bar{L}=\rho R^2\bar{c}\Phi n\left[-\frac{1}{2}\frac{\partial C_L}{\partial\gamma_y}\overline{\cos^2(\phi)\left|\frac{d\hat{\phi}}{d\hat{t}}\right|}\hat{r}_3^3(S)R+\hat{r}_1^1(S)l_1\overline{C_D(\alpha_0)\sin^2(\phi)\left|\frac{d\hat{\phi}}{d\hat{t}}\right|}+\frac{1}{2}l_1\frac{\partial C_D}{\partial\mu_y}\overline{\sin^2(\phi)\left|\frac{d\hat{\phi}}{d\hat{t}}\right|}\hat{r}_2^2(S)\right]v. \tag{33}$$

During lateral translation, the spanwise flow for the left and right wings is always modified in an opposite manner [as shown in Fig. 2(b)]. For example, when moving to the right, the flow for the left wing is enhanced, and for the right wing, it is reduced; thus, the right wing is expected to generate less lift (or more, depending on the sign of $\partial C_L/\partial\gamma_y$) than the left wing, which leads to a roll torque.

With the aforementioned modifications to the analytical models, the value of the stability derivatives X_u^+, M_u^+, Y_v^+, and L_v^+ will be changed accordingly. The results are strongly dependent on the values of $\partial C_D/\partial\mu$ and $\partial C_L/\partial\gamma$. An estimation of $\partial C_D/\partial\mu$ can be obtained by the use of [22, (25) and (26)]. Note that $\partial C_D/\partial\mu$ is a function of α and normally has negative values, i.e., because a positive μ tends to reduce the force coefficient. Therefore, by taking into account the chordwise change of the sectional velocity that is induced by body translation, we find that (30) and (32) predict lower values than those by (4) and (8). For example, the stability derivatives X_u^+ and Y_v^+ are

reduced by 34% and 36% for fruit fly, i.e., $X_u^+ = -0.98$, and $Y_v^+ = -0.89$. However, the variations of X_u^+ and Y_v^+ barely affect the overall dynamics of the system, because the values of X_u/m and Y_v/m in the system matrix (27) are much smaller than the other dominant terms.

As mentioned, it is still not well known how additional spanwise flow (which results from body motion) will change the vortex structure and force production. As found by recent CFD studies [16], additional spanwise flow from wing base to tip tends to enhance the lift production, therefore, suggesting that $\partial C_L/\partial\gamma$ has positive values. We can see that in (31), during a forward translation, a nose-up pitching is induced by the drag force that is directed backward (second and third terms in the parentheses). The term that is associated with $\partial C_L/\partial\gamma$ tends to create a nose-down torque, thereby reducing the total nose-up torque. However, the effect of $\partial C_L/\partial\gamma$ on the stability derivative M_u^+ might be limited, especially, for low-stroke amplitude insects [term $\sin^2(\phi)$ is small; see (31)].

On the other hand, $\partial C_L/\partial\gamma$ may have considerable effect on L_v because the roll torque is at a maximum during midstrokes when spanwise flow is most affected by the body lateral velocity. From (33), we can see that the term that is associated with $\partial C_L/\partial\gamma$ tends to produce a torque that is opposite from the direction of torque that is induced by lateral drag. If it is more dominant than the drag-induced roll torque, it will result in a negative L_v^+ (according to the coordinate system that is defined in the current study). It can be shown that a negative L_v^+ will lead to lateral dynamics containing a stable fast-subsidence mode, a stable slow-oscillatory mode, and an unstable slow-divergence mode, which are consistent to those from CFD results on lateral dynamics. However, no conclusion can be made here because of the lack of an accurate estimation of $\partial C_L/\partial\gamma$ and the understanding of the effect of additional spanwise flow on force production.

B. Wing Rotation and Wing–Wake Interaction

It is well known that the translational component of aerodynamic force because of delayed stall mechanism [6] contributes to most of the total force, especially around midstrokes. Near stroke reversals, however, force transients are largely determined by rotational lift (Kramer effect) and wake-capture mechanisms [3], which are not considered in the analytical models. Therefore, in this section, we discuss how wing kinematics are changed (by body movements) during stroke reversals and how unsteady mechanisms are affected.

As shown in Fig. 3(a), body translations will delay or bring forward stroke reversals when changing the relative timing of wing rotation. For example, when moving backward [see Fig. 3(a.i)], the ventral stroke reversal is delayed, and this leads to an advanced wing rotation (assuming a symmetrical wing rotation without body motion). On the other hand, the dorsal stroke reversal [see Fig. 3(a.ii)] is brought forward and results in an advanced wing rotation. As shown by Dickinson *et al.* [6], an advanced wing rotation will significantly increase the lift produced because of an enhanced wing–wake interaction after the stroke reversal. On the contrary, delayed wing rotation reduces

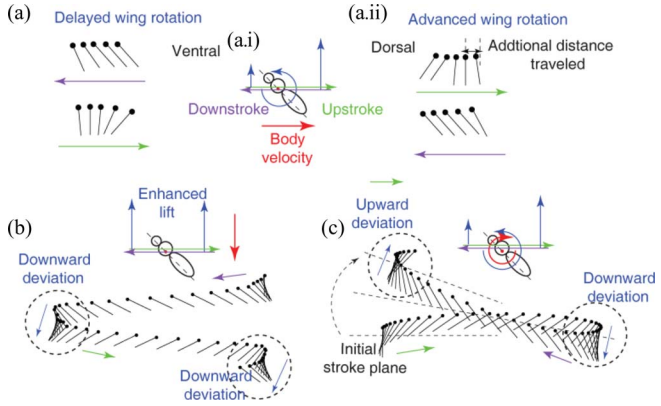

Fig. 3. Schematic illustrations of the effective wing kinematics relative to the global frame. (a) Body is moving backward. (a.i) Wing kinematics during ventral stroke reversal—less distance is traveled, which results in delayed rotation. (a.ii) Wing kinematics during dorsal stroke reversal—additional distance is traveled because of the overall backward motion, which results in advanced wing rotation. (b) Wing trajectory during vertical descent—wing moves downward at both ventral and dorsalstroke reversals. (c) Wing trajectory during nose-up pitching—wing moves downward at dorsal stroke reversal and upward at ventral stroke reversal. The solid black line denotes the wing chord, with the filled cycle that marks the leading edge.

the wing–wake interaction and lowers lift production. Therefore, we can see that a backward translation will induce a large pitch-down moment [see the blue arrow in Fig. 3(a)], especially when the moment arm for the pitch torque is at maximum during stroke reversals. This indicates that (5) may underestimate the pitch torque and that a higher value of M_u^+ is expected. Similar effects may also take place for lateral translation; however, since moment arm for the roll torque is at minimum at stroke reversals, it may have very limited effect, and (9) is still a good approximation.

Furthermore, body movements also affect the wing–wake interaction by the induction of effective wing deviations. For example, during vertical descent, the wing is moving downward after both ventral and dorsal stroke reversals [see Fig. 3(b)], therefore, enhancing the wing–wake interaction [9]. However, it is still not known how descending motion affects the wing–wake interaction during midstrokes; thus, the overall effect cannot be determined without further investigations. On the other hand, during a pitch rotation [e.g., a nose-up pitching in Fig. 3(c)] we can see that an upward deviation occurs at the ventral stroke reversal, and a downward deviation occurs at the dorsal stroke reversal. Therefore, the lift force is enhanced at the dorsal side and reduced at the ventral side. Because at stroke reversals the moment arm for the pitch torque is at maximum, we expect that a large amount of pitch FCT is produced against the pitch rotation. This is confirmed by results from a dynamically scaled robotic wing experiment, as shown in Fig. 4(b). (For more details about robotic wing experiments, see [29].) We can see that the pitch torque at the beginning upstroke [after ventral stroke reversal see the blue curve in Fig. 4(b.i)] is reduced, and the one at the beginning of the downstroke is enhanced [after dorsal stroke reversal; see the red curve in Fig. 4(b.i)]. Therefore, the total pitch FCT [see the green curve in Fig. 4(b.i)] is greatly enhanced, compared with the prediction by (21). The stroke-averaged

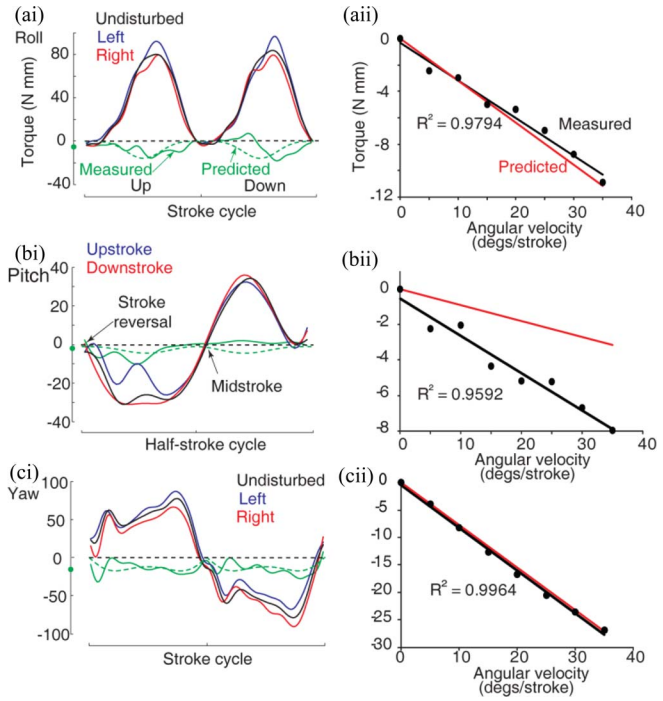

Fig. 4. FCTs measured in robotic wing experiments ($Re = 800$). (a.i), (b.i), and (c.i) Time courses of FCTs (angular velocity at 20°/stroke), which are shown by the solid green curves and the filled green cycles on the ordinates, represent their averages. The predicted torques by the analytical models are shown by a dotted green curve. The black curves represent the torques measured when there is no body rotation (undisturbed). (a.ii), (b.ii), and (c.ii) Stroke-averaged values as a function of the angular velocity. Measured and predicted torques are shown in black and red, respectively. (a) Roll rotation; torques generated by the left and right wings are shown by the blue and red curves. The roll torque of the left wing is plotted oppositely (relative to the horizontal zero axis). Therefore, the total torque (green) is obtained by subtracting the blue curve from the red curve. (b) Pitch rotation; torques during up- and downstrokes are shown by the blue and red curves. The pitch torque during upstroke is plotted oppositely. (c) Yaw rotation; torques that are generated by the left and right wings are shown by the blue and red curves. The yaw torque of the left wing is plotted oppositely.

values as a function of the angular velocity are shown in Fig. 4(b.ii), and the estimation of M_q^+ accounts for only 30% of the actual value. Compared with FCT during pitch rotation, it is less affected during roll rotation because at stroke reversals the moment arm for the roll torque is at minimum; thus, the prediction by (18) agrees well with the measured one, as shown in Fig. 4(a.ii) (A plot of instantaneous values is shown in Fig. 4(a.i).) At last, for a yaw rotation, the stroke plane is fixed, and there is no induced wing deviation. Therefore, not surprisingly, the predictions by (22) and (23) agree well with the experimental results [see Fig. 4(c)].

C. Additional Modeling Error and Effects on the Results

To derive (5) and (9), which are associated with the stability derivatives M_q^+ and L_v^+, we neglected the translational velocity of the stroke plane, which is induced by body rotations (roll and pitch) around the center of mass. During a rotation around the body roll axis, for example, the stroke plane rotates about its roll axis and translates along the pitch axis. The latter will further impart an amount of roll countertorque (similar to the production of L_v^+) around the center of mass. The amount of the stability derivative that is neglected can be estimated by

$$\tilde{M}_q^+ = M_u^+ \frac{\hat{L}\hat{l}_1}{2\Phi\hat{r}_2} \tag{34}$$

$$\tilde{L}_q^+ = L_v^+ \frac{\hat{L}\hat{l}_1}{2\Phi\hat{r}_2} \tag{35}$$

where $\hat{L}$ is the ratio of body and wing lengths. By the use of fruit fly data, we can find $\tilde{M}_q^+ \approx 0.08 M_u^+$. We note that the effect of M_q^+ (L_p^+) on the flight dynamics is relatively small. If we increase the value of M_q^+ by fourfold, for example, the changes in the resulting dynamics are still minor (i.e., by the use of stalk-eyed fly data, we find that the maximum change of the eigenvalues is within 15%). Therefore, we consider that the errors in the estimations of stability derivatives M_q^+ and L_p^+ have very limited effects on our results.

Furthermore, how FCTs depend on accelerations is still undetermined. Although the FCT and FCF models can be used to estimate the first derivatives with respect to time, e.g., X_u, we are unable to estimate the second derivatives, e.g., $X_{\dot{u}}$. For fixed and rotary aircraft, such stability derivatives are important under some flight conditions (e.g., short-period mode), in which the associated time constant is so short that the acceleration becomes critical to aerodynamics [28]. However, in hover, it is still well approximated that the first derivatives dominate the aerodynamics [24], [28].

As we have seen, a better understanding of the effects of spanwise flow and wing–wake interaction will help to model the flight dynamics more accurately. Dynamically scaled robotic wing experiments or computational studies on qualifying these effects are desirable in future studies. As an approximation of the flight dynamics, however, our models provide an applicable and simple analytical tool, which is important to design the controllers for the flapping-wing micro air vehicles (MAVs) (e.g., see [30]), as well as to understand the control strategies that are adapted by flying insects.

V. Conclusion and Future Works

In this paper, we have derived the full 6-DOF body dynamics of flapping flight near hover by the incorporation of the analytical models for the newly found FCTs and FCFs, which are aerodynamic torques and forces that are produced by flapping-wing fliers from the effects of body rotational and translational motions. We have found that these damping terms are always in the opposite direction of motion and are linearly proportional to the body velocity and wing beat frequency. Experimental results have been performed to validate these models, which were then applied to estimate the stability derivatives that are associated with the 6-DOF flight dynamics, which is linearized at hover. The flight dynamics of four species of flapping-wing insects have been analyzed for their dynamic stability on the basis of our analytical models. We found that, consistent with previous studies, some subsets of the dynamic modes are passively stable.

The first major contribution of this study is to derive the principles and theoretical models of the FCTs and FCFs, which is an important property that is uniquely associated with flapping

flight. They result in significant damping in system dynamics and are the inherent properties of flapping flight. As an extension of our recent work on yaw-turn models, we include, in this study, all the rotational and translational damping along six principle axes: roll, pitch, yaw, forward/backward, sideways, and heave. Analytical models along with experimental results through robotic wing tests and real insect flight data further validated the theory. The significant damping in flapping flight implies passive stability under external disturbances, such as wind gust, and coupled with active control, it allows the insect or robotic flyers stable yet maneuverable flight.

The second major contribution of this study is to provide a revised analytical form of flapping flight dynamics at hover. It can be used very easily to study the flight dynamics by the use of the available morphological and kinematic data (as we did in Section III) and to explain the observed flight behavior of flapping-wing animals. Similarly, this model can be easily applied to estimate the dynamics of a flapping-wing MAV prototype and investigate the effects of design parameters (wing length, center of mass, moment of inertia, etc.) on the flight stability and performance. In the meanwhile, the estimation of the damping characteristics (when the robot is translating or rotating in the air) helps to determine the amount of wing kinematic changes required that can achieve certain flight performance (e.g., maximum turning rate, cursing speed, etc.). The knowledge of the flight dynamics is helpful in the design of the control mechanisms, which can then be chosen to stabilize the unstable modes. The current model can also be easily expanded to include control inputs, and then, "closed-loop" dynamics can be derived accordingly [30].

As a parallel work on the experimental front, the analytical model derived in this study is applied to estimate the translational damping characteristics of a pair of life-size robotic insect wings that are developed in the lab [31]. The analytical results are in good agreement with the experimental measurements on the wings. For future works, it is important to apply the theory and model found in this study to the design and parameter selection of the flapping-wing robotic insect that can achieve stable and maneuverable hovering through passive dynamic stability and active flight control.

Meanwhile, the current analytical model are from simple first-order analysis; it can be further expanded to include more complicated wing kinematic parameters, such as stroke plane tilt angle, stroke angle offset, and wing deviation, which are usually presented in real flying insects [32]. Similarly, as mentioned at the end of Section IV, additional experiments on dynamically scaled robotic wings are needed to expand these models by the incorporation of detailed understanding of the neglected aerodynamic effects, such as wake capture and wing rotational force.

APPENDIX A

DERIVATIONS OF ANALYTIC MODELS: FLAPPING COUNTERFORCE AND FLAPPING COUNTERTORQUE

In this Appendix, we provide detailed derivations of analytical models for aerodynamic damping during body translations along and body rotations about the principal axes of the stroke plane frame. Forces and torques are calculated based on the quasi-steady aerodynamic model [6], [22].

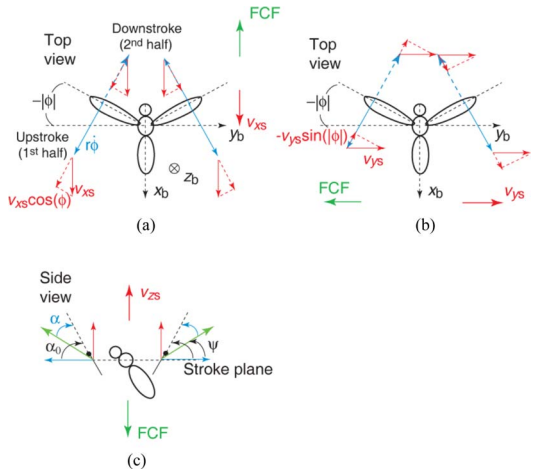

Fig. 5. Schematic view of FCF production during (a) backward, (b) rightward, and (c) upward translations. Blue arrows denote the directions of the wing velocity (solid for the first half of upstroke and dashed for the srcond half of downstroke), and red arrows denote the body translational velocity.

Fig. 5 summarizes the changes of wing velocity and angle of attack during body translations. In the following, we derive the analytical models of FCFs case by case.

FORWARD/BACKWARD TRANSLATION

Based on blade-element analysis, it can be shown that the mean aerodynamic force that acts on a wing is given by

$$\begin{aligned} F(\hat{t}) &= \frac{1}{8}\rho R^3 \bar{c}\Phi^2 n^2 C_F(\alpha, \mu_x, \gamma_x)\left(\frac{d\hat{\phi}}{d\hat{t}}\right)^2 \\ &\quad \times (\hat{r}_2^2(S) + 2\hat{r}_1^1(S)\mu_x + \mu_x^2) \\ &\approx \frac{1}{8}\rho R^3 \bar{c}\Phi^2 n^2 \left[C_F(\alpha_0) + \frac{\partial C_F}{\partial \gamma_x}\gamma_x + \frac{\partial C_F}{\partial \mu_x}\mu_x\right]\left(\frac{d\hat{\phi}}{d\hat{t}}\right)^2 \\ &\quad \times (\hat{r}_2^2(S) + 2\hat{r}_1^1(S)\mu_x + \mu_x^2) \end{aligned} \tag{A1}$$

where we approximate $C_F(\alpha, \mu_x, \gamma_x)$ by $C_F(\alpha_0) + (\partial C_F/\partial\gamma_x)\gamma_x + (\partial C_F/\partial\mu_x)\mu_x$. From Fig. 5(a), we can see that, during a backward translation, the drag force is reduced when wing velocity is directed opposite the direction of translation (during downstrokes, μ_x is negative) and enhanced when directed in the same direction of translation (during upstrokes, μ_x is positive). Specifically, we note the following.

During downstrokes:

μ_x: negative for dorsal-to-mid stroke (first half of downstroke) and negative for mid-to-ventral stroke (second half of downstroke);

γ_x: negative for dorsal-to-mid stroke and positive for mid-to-ventral stroke.

During upstrokes:

μ_x: positive for ventral-to-mid stroke (first half of upstroke) and positive for mid-to-dorsal stroke (second half of upstroke);

γ_x: positive for ventral-to-mid stroke and negative for mid-to-dorsal stroke.

Therefore, the stroke-averaged drag of a wing pair along x_s axis is

$$\begin{aligned}\overline{F_D} = \bar{X} &= \frac{1}{2}[\overline{F_{D-d1}\cos(\phi)} + \overline{F_{D-d2}\cos(\phi)} \\ &\quad + \overline{F_{D-u1}\cos(\phi)} - \overline{F_{D-u2}\cos(\phi)}] \\ &= -\rho R^2 \bar{c}\Phi n \left[\hat{r}_1^1(S)\overline{C_D(\alpha_0)\cos^2(\phi)\left|\frac{d\hat{\phi}}{d\hat{t}}\right|}\right. \\ &\quad \left. + \frac{1}{2}\frac{\partial C_D}{\partial \mu_x}\overline{\cos^2(\phi)\left|\frac{d\hat{\phi}}{d\hat{t}}\right|}\hat{r}_2^2(S)\right] v_{xs}. \end{aligned} \tag{A2}$$

In the meantime, there is a pitch moment that is produced around body center of mass resulting from the imbalance of lift force:

$$\begin{aligned}\overline{\tau_{\text{pitch}}} = \bar{M} &= \frac{1}{2}[-\overline{F_{L-d1}|\sin(\phi)|} + \overline{F_{L-d2}|\sin(\phi)|} \\ &\quad + \overline{F_{L-u1}|\sin(\phi)|} - \overline{F_{L-u2}|\sin(\phi)|}]Rr_{cp} + \overline{F_D}l_1 \\ &= \rho R^2 \bar{c}\Phi n \left[\frac{1}{2}\frac{\partial C_L}{\partial \gamma_x}\overline{\sin^2(\phi)\left|\frac{d\hat{\phi}}{d\hat{t}}\right|}\hat{r}_3^3(S)R - \hat{r}_1^1(S)\right. \\ &\quad \times l_1\overline{C_D(\alpha_0)\cos^2(\phi)\left|\frac{d\hat{\phi}}{d\hat{t}}\right|} \\ &\quad \left. -\frac{1}{2}l_1\frac{\partial C_D}{\partial \mu_x}\overline{\cos^2(\phi)\left|\frac{d\hat{\phi}}{d\hat{t}}\right|}\hat{r}_2^2(S)\right] v_{xs} \end{aligned} \tag{A3}$$

where the subscript $d1$ denotes the first half of downstroke, $u2$ denotes the second half of upstroke, and so forth; and the subscript L refers to the lift force. We also approximated $\hat{r}_2^2(S)r_{cp}$ by $\hat{r}_3^3(S)$ according to blade-element analysis.

Lateral Translation

We can see in Fig. 5(b) that during a lateral motion to the right (left), the net drag of a wing pair along the pitch axis y_s is always pointing to the left (right) at any instant of time. Specifically, we note the following.

During the first half of downstroke:

μ_y: negative for the left wing and positive for the right wing;

γ_y: positive for the left wing and negative for the right wing.

Then, the drag force along lateral axis y_s is

$$F_D(\hat{t}) = [F_{D-l}(\hat{t}) - F_{D-r}(\hat{t})]|\sin(\phi)| \tag{A4}$$

where the subscript $D-l$ refers to the drag of left wing, and so forth.

During the second half of downstroke:

μ_y: positive for the left wing and negative for the right wing;

γ_y: positive for the left wing and negative for the right wing.

Therefore, we have

$$F_D(\hat{t}) = [-F_{D-l}(\hat{t}) + F_{D-r}(\hat{t})]|\sin(\phi)|. \tag{A5}$$

During the first half of upstroke:

μ_y: negative for the left wing and positive for the right wing;

γ_y: positive for the left wing and negative for the right wing.

Therefore, we have

$$F_D(\hat{t}) = [F_{D-l}(\hat{t}) - F_{D-r}(\hat{t})]|\sin(\phi)|. \tag{A6}$$

During the second half of upstroke:

μ_y: positive for the left wing and negative for the right wing;

γ_y: positive for the left wing and negative for the right wing.

Therefore, we have

$$F_D(\hat{t}) = [-F_{D-l}(\hat{t}) + F_{D-r}(\hat{t})]|\sin(\phi)|. \tag{A7}$$

The formula for $F_D(\hat{t})$ is (A1) with the subscript x replaced by y. Then, it can be shown that the averaged drag along axis y_s is

$$\begin{aligned}\overline{F_D} = \bar{Y} &= -\rho R^2 \bar{c}\Phi n \left[\hat{r}_1^1(S)\overline{C_D(\alpha_0)\left|\frac{d\hat{\phi}}{d\hat{t}}\right|\sin^2(\phi)}\right. \\ &\quad \left. + \frac{1}{2}\frac{\partial C_D}{\partial \mu_y}\overline{\sin^2(\phi)\left|\frac{d\hat{\phi}}{d\hat{t}}\right|}\hat{r}_2^2(S)\right] v_{ys}. \end{aligned} \tag{A8}$$

The roll torque around body center of mass is calculated by

$$\begin{aligned}\overline{\tau_{\text{roll}}} = \bar{L} &= [-\overline{F_{L-l}\cos(\phi)} + \overline{F_{L-r}\cos(\phi)}]Rr_{cp} + \overline{F_D}l_1 \\ &= \rho R^2 \bar{c}\Phi n \left[-\frac{1}{2}\frac{\partial C_L}{\partial \gamma_y}\overline{\left|\frac{d\hat{\phi}}{d\hat{t}}\right|\cos^2(\phi)}\hat{r}_3^3(S)R\right. \\ &\quad + \hat{r}_1^1(S)l_1\overline{C_D(\alpha_0)\left|\frac{d\hat{\phi}}{d\hat{t}}\right|\sin^2(\phi)} \\ &\quad \left. + \frac{1}{2}l_1\frac{\partial C_D}{\partial \mu_y}\overline{\sin^2(\phi)\left|\frac{d\hat{\phi}}{d\hat{t}}\right|}\hat{r}_2^2(S)\right] v_{ys}. \end{aligned} \tag{A9}$$

A. Vertical Translation

During a vertical ascent [see Fig. 5(c)], the sectional lift force is given by

$$dF_L(\hat{t}) = \frac{1}{2}\rho(dr)c(r)C_N(\alpha_0 - \psi)\cos(\alpha_0)\left(\frac{r|d\phi/dt|}{\cos(\psi)}\right)^2 \tag{A10}$$

where the force coefficient is only dependent on the angle of attack (chordwise and spanwise tip velocity ratios both equal zero). The change of the sectional lift force that results from vertical velocity is

$$\begin{aligned}\Delta dF_L(\hat{t}) &= \frac{1}{2}\rho(dr)c(r)C_N(\alpha_0 - \psi)\cos(\alpha_0)\left(\frac{r|d\phi/dt|}{\cos(\psi)}\right)^2 \\ &\quad - \frac{1}{2}\rho(dr)c(r)C_N(\alpha_0)\cos(\alpha_0)\left(\frac{r|d\phi/dt|}{dt}\right)^2 \\ &= \frac{1}{2}\rho(dr)c(r)\left(r\left|\frac{d\phi}{dt}\right|\right)^2\cos(\alpha_0) \\ &\quad \times \left[C_N(\alpha_0 - \psi)\left(\frac{1}{\cos(\psi)}\right)^2 - C_N(\alpha_0)\right] \end{aligned} \tag{A11}$$

where $C_N(\alpha_0 - \psi)$ is approximated as in (12). We have

$$\Delta dF_L(\hat{t}) \approx -\frac{1}{2}\rho(dr)c(r)r\left|\frac{d\phi}{dt}\right|\cos(\alpha_0)\left[\frac{dc_N(\alpha)}{d\alpha}_{|\alpha=\alpha_0} v_{zs}\right]. \tag{A12}$$

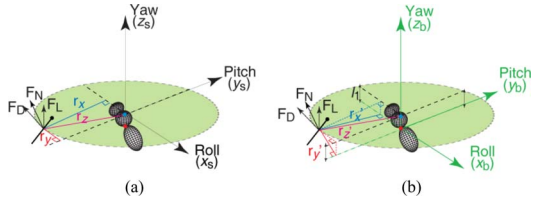

Fig. 6. Coordinate frames and moment of arms. (a) Schematic view of an insect body with a wing chord, showing stroke plane reference frame axes roll x_s, pitch y_s, and yaw z_s; normal force F_N, drag F_D, and lift F_L; $F_N = \sqrt{F_D^2 + F_c^2}$. The moment of arms relative to the wing base are r_x, r_y, and r_z for roll, pitch, and yaw torques, respectively. Note that $r_z = r$ (spanwise position of the wing chord), $r_x = \cos(\phi) r_z$, and $r_y = \sin(\phi) r_z$. (b) Insect body with the body coordinate frame roll x_b, pitch y_b, and yaw z_b. r'_x, r'_y, and r'_z are distances from the wing section to each of the principal axes of the body frame; the corresponding orthogonal distances are the same as r_x, r_y, and r_z in (a), indicating that the moment arms relative to the center of mass are identical to those relative to the wing base.

Integrate the previous equation over the wingspan, and we have the net lift change of a wing pair:

$$\begin{aligned}\Delta F_L(\hat{t}) &= -\frac{1}{2}\rho R^2 \bar{c}\Phi n \left|\frac{d\hat{\phi}}{d\hat{t}}\right| \cos(\alpha_0) \frac{dC_N(\alpha)}{d\alpha}_{|\alpha=\alpha_0} \\ &\quad \times \left(\int_0^1 (d\hat{r})\hat{c}(r)\hat{r}\right) v_{zs} \\ &= -\frac{1}{2}\rho R^2 \bar{c}\Phi n \left|\frac{d\hat{\phi}}{d\hat{t}}\right| \cos(\alpha_0) \frac{dC_N(\alpha)}{d\alpha}_{|\alpha=\alpha_0} \hat{r}_1^1(S) v_{zs}.\end{aligned} \tag{A13}$$

The stroke-averaged value is (also applies to descending)

$$\overline{\Delta F_L} = \bar{Z} = -\frac{1}{2}\rho R^2 \bar{c}\hat{r}_1^1(S)\Phi n \overline{\frac{dC_N}{d\alpha}_{|\alpha=\alpha_0} \cos(\alpha_0) \left|\frac{d\hat{\phi}}{d\hat{t}}\right|} v_{zs}. \tag{A14}$$

Next, analytical models for FCTs are derived, and the moment arms for roll, pitch, and yaw torques are shown in Fig. 6.

Roll Rotation

As indicated by Fig. 7, rotation around the roll axis x_s adds a downward velocity (always normal to the stroke plane) to the left wing, while increasing its effective angle of attack α. On the contrary, it adds an upward velocity to the right wing and reduces its effective angle of attack.

We write the lifts that are produced at a wing section of left and right wings, respectively, as

$$dF_{L-l}(\hat{t}, r) = \frac{1}{2} C_N(\alpha_0 + \psi) \cos(\alpha_0) \rho (dr) c r^2 \left(\frac{|d\phi/dt|}{\cos(\psi)}\right)^2 \tag{A15}$$

and

$$dF_{L-r}(\hat{t}, r) = \frac{1}{2} C_N(\alpha_0 - \psi) \cos(\alpha_0) \rho (dr) c r^2 \left(\frac{|d\phi/dt|}{\cos(\psi)}\right)^2 \tag{A16}$$

where α_0 is the geometric angle of attack that is determined by wing kinematics, ψ (15) is the angle between the stroke plane and the total wing velocity U (16), and the lift coefficient (only a function of the angle of attack) is approximated by $C_N(\alpha_0 + \psi)\sin(\varphi)$. Then, the roll torques that are produced by left and right wings (at a wing section) are calculated, respectively, as

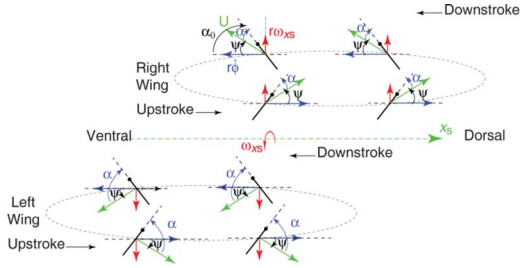

Fig. 7. Schematic view of FCT production for roll rotation. $r\dot{\phi}$ is the velocity that results from wing motion (blue arrows), $r\omega_{xs}$ is the velocity that is induced by body rotation (red arrows), and U is the total velocity (green arrows). The angle between the stroke plane and the wing chord is denoted as α_0 (the geometric angle of attack, i.e., the angle between the blue arrow and the dashed line parallel to the wing chord, only shown on top left); the angle between the stroke plane and the wing velocity is denoted as ψ; the effective angle of attack α is the angle between the total velocity U and the wing chord. This is a 2-D projection of a 3-D kinematic pattern, viewed in the chordwise direction from wing tip to wing base for the left wing and from wing base to wing tip for the right wing.

$$d\tau_{\text{roll}-l}(\hat{t}, r) \approx -\frac{1}{2} C_N(\alpha_0 + \psi) \cos(\alpha_0) \rho (dr) c r^3 \left|\frac{d\phi}{dt}\right|^2 \cos(\phi) \tag{A17}$$

and

$$d\tau_{\text{roll}-r}(\hat{t}, r) \approx \frac{1}{2} C_N(\alpha_0 - \psi) \cos(\alpha_0) \rho (dr) c r^3 \left|\frac{d\phi}{dt}\right|^2 \cos(\phi). \tag{A18}$$

We approximate $C_N(a_0 \pm \psi)$ as in (12); then, the total roll torque is

$$\begin{aligned} d\tau_{\text{roll}}(\hat{t}, r) &= d\tau_{\text{roll}-l}(\hat{t}) + d\tau_{\text{roll}-r}(\hat{t}, r) \\ &= -\frac{dC_N(\alpha)}{d\alpha}_{|\alpha_0} \psi \cos(\alpha_0) \rho (dr) c r^3 \left|\frac{d\phi}{dt}\right|^2 \cos(\phi). \end{aligned} \tag{A19}$$

By the integration over the wingspan, we have the total roll torque that is produced by a wing pair:

$$\begin{aligned} \tau_{\text{roll}}(\hat{t}) &= -\frac{dC_N(\alpha)}{d\alpha}_{|\alpha_0} \psi R^4 \bar{c} \cos(\alpha_0) \rho \left|\frac{d\phi}{dt}\right|^2 \\ &\quad \times \cos(\phi) \int_0^1 \hat{r}^3 \hat{c} d\hat{r} \\ &= -\frac{1}{2}\rho R^4 \bar{c} \hat{r}_3^3(S) \frac{dC_N(\alpha)}{d\alpha}_{|\alpha_0} \cos(\alpha_0) \\ &\quad \times \cos^2(\phi) \left|\frac{d\hat{\phi}}{d\hat{t}}\right| \Phi n \omega_{xs} \end{aligned} \tag{A20}$$

which is the FCT for roll rotation at a nondimensional time $\hat{t}$. The averaged value over one wing stroke is

$$\begin{aligned} \overline{\tau_{\text{roll}}} = \bar{L} &= -\frac{1}{2}\rho R^4 \bar{c} \hat{r}_3^3(S) \\ &\quad \times \overline{\frac{dC_N(\alpha)}{d\alpha}_{|\alpha_0} \cos(\alpha_0) \cos^2(\phi) \left|\frac{d\hat{\phi}}{d\hat{t}}\right|} \Phi n \omega_{xs}. \end{aligned} \tag{A21}$$

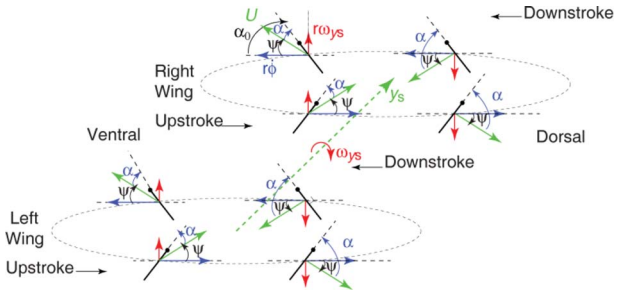

Fig. 8. Schematic view of FCT production for pitch rotation. See the legend of Fig. 7 for details.

Moreover, it is easy to see from Fig. 7 that for up- and downstrokes of a single wing, the lift-force generation is geometrically symmetric with respect to the midstroke; thus, the averaged pitch torque is zero over one wing stroke:

$$\overline{\tau_{\text{pitch}}} = 0. \tag{A22}$$

Similarly, the drag-force generation is geometrically symmetric between up- and downstrokes, and the total yaw torque is zero when averaged over a complete wing stroke:

$$\overline{\tau_{\text{yaw}}} = 0. \tag{A23}$$

Pitch Rotation

As shown in Fig. 8, for either the left or the right wing, the effective angle of attack α is enhanced during the first half of downstroke (dorsal-to-middle stroke) and the second half of upstroke (middle-to-dorsal stroke), and it is reduced during the second half of downstroke (middle-to-ventral stroke) and the first half of upstroke (ventral-to-middle stroke). Therefore, when the wing is located at the dorsal half of the stroke plane, the instantaneous lift at a wing section of a single wing (i.e., left wing) can be written as

$$dF_{L-l-\text{dorsal}}(\hat{t}, r) = \frac{1}{2} C_N(\alpha_0 + \psi)\cos(\alpha_0)\rho(dr)cr^2 \times \left(\frac{|d\phi/dt|}{\cos(\psi)}\right)^2. \tag{A24}$$

Similarly, when the wing is located at the ventral half of the stroke plane, the instantaneous lift at a wing section of a single wing (i.e., left wing) is written as

$$dF_{L-l-\text{ventral}}(\hat{t}', r) = \frac{1}{2} C_N(\alpha_0 - \psi)\cos(\alpha_0)\rho(dr)cr^2 \times \left(\frac{|d\phi/dt|}{\cos(\psi)}\right)^2. \tag{A25}$$

Then, we have the pitch torques

$$d\tau_{\text{pitch}-l-\text{dorsal}}(\hat{t}, r) = -\frac{1}{2} C_N(\alpha_0 + \psi)\cos(\alpha_0)\rho(dr)cr^3 \times \left(\frac{|d\phi/dt|}{\cos(\psi)}\right)^2 \sin(\phi) \tag{A26}$$

and

$$d\tau_{\text{pitch}-l-\text{ventral}}(\hat{t}', r) = \frac{1}{2} C_N(\alpha_0 - \psi)\cos(\alpha_0)\rho(dr)cr^3 \times \left(\frac{|d\phi/dt|}{\cos(\psi)}\right)^2 \sin(\phi). \tag{A27}$$

Next, we approximate $C_N(\alpha_0 \pm \psi)$, as in (12), and sum (A26) and (A27) as

$$d\tau_{\text{pitch}-l-\text{dorsal}}(\hat{t}, r) + d\tau_{\text{pitch}-l-\text{ventral}}(\hat{t}', r) \approx -\frac{dC_N(\alpha)}{d\alpha}_{|\alpha_0} \psi\, \cos(\alpha_0)\rho(dr)cr^3 \left|\frac{d\phi}{dt}\right|^2 \sin(\phi). \tag{A28}$$

By the integration over the wingspan, we have

$$\tau_{\text{pitch}-l-\text{dorsal}}(\hat{t}) + \tau_{\text{pitch}-l-\text{ventral}}(\hat{t}') = -\frac{1}{2}\rho R^4 \bar{c}\hat{r}_3^3(S) \times \frac{dC_N(\alpha)}{d\alpha}_{|\alpha_0} \cos(\alpha_0)\sin^2(\phi)\left|\frac{d\hat{\phi}}{d\hat{t}}\right| \Phi n\omega_{ys}. \tag{A29}$$

We then have the averaged pitch torque of a wing pair over a complete stroke:

$$\overline{\tau_{\text{pitch}}} = \bar{M} = \overline{\tau_{l-\text{pitch}}} + \overline{\tau_{r-\text{pitch}}} = -\frac{1}{2}\rho R^4 \bar{c}\hat{r}_3^3(S) \times \overline{\frac{dC_N(\alpha)}{d\alpha}_{|\alpha_0} \cos(\alpha_0)\sin^2(\phi)\left|\frac{d\hat{\phi}}{d\hat{t}}\right|} \Phi n\omega_{ys}. \tag{A30}$$

Furthermore, it is easy to see that during pitch rotation, the left and right wings have symmetric wing motions (see Fig. 7); therefore, symmetric torque generations around the roll and pitch axes are expected:

$$\overline{\tau_{\text{roll}}} = 0 \tag{A31}$$

$$\overline{\tau_{\text{yaw}}} = 0. \tag{A32}$$

Yaw Rotation

During yaw rotation of the stroke plane, there is no change in the effective angle of attack but only in wing velocities. The stroke-averaged FCT is [18], [19], [23]

$$\overline{\tau_{\text{yaw}}} = \bar{N} = -\rho R^4 \bar{c}\hat{r}_3^3(S)\Phi n \overline{C_D(\alpha_0)\left|\frac{d\hat{\phi}}{d\hat{t}}\right|}\omega_{zs}. \tag{A33}$$

If we approximate $C_D(\alpha_0)$ by $C_N(\alpha_0)\cos(\varphi)$, it becomes

$$\overline{\tau_{\text{yaw}}} = \bar{N} = -\rho R^4 \bar{c}\hat{r}_3^3(S)\Phi n \overline{C_N(\alpha_0)\cos(\varphi)\left|\frac{d\hat{\phi}}{d\hat{t}}\right|}\omega_{zs} \tag{A34}$$

where ω_{zs} is the yaw angular velocity.

APPENDIX B

TABLE II
INSECT MORPHOLOGICAL AND WING KINEMATIC DATA

Species	Mass (g)	I_{xx} (Nms^2)	I_{yy} (Nms^2)	I_{zz} (Nms^2)	I_{xz} (Nms^2)	χ_0 (°)	$\hat{l}_1$ (-)	L (mm)	R (mm)	$\bar{c}$ (mm)	n (Hz)	Φ (°)	$\hat{r}_1(S)$ (-)	$\hat{r}_2(S)$ (-)	$\hat{r}_3(S)$ (-)
Fruit fly (*Drosophila melanogaster*)	9.6 $\times 10^{-4}$	3.06 $\times 10^{-13}$	5.06 $\times 10^{-13}$	3.06 $\times 10^{-13}$	-1.91 $\times 10^{-13}$	45	0.20	2.5	2.39	0.8	218	140	0.49	0.545	0.59
Hawkmoth (*Manduca sexta*)	1.62	2.55 $\times 10^{-7}$	2.83 $\times 10^{-7}$	2.43 $\times 10^{-7}$	-3.34 $\times 10^{-8}$	50	0.27	39.5	48.8	18.6	26	98	0.435	0.505	0.56
Stalk-eyed fly (*Cyrtodiopsis dalmanni*)	7.00 $\times 10^{-3}$	2.67 $\times 10^{-11}$	2.95 $\times 10^{-11}$	8.48 $\times 10^{-12}$	-7.65 $\times 10^{-12}$	70	0.25	6.23	4.46	0.94	170	140	0.568	0.614	0.64
Bumblebee (*Bombus*)	0.175	3.70 $\times 10^{-9}$	2.13 $\times 10^{-9}$	2.08 $\times 10^{-9}$	-1.73 $\times 10^{-9}$	57.5	0.21	18.6	13.2	4.01	155	116	0.49	0.55	0.60

$l_1 = \hat{l}_1 L$, where L is the body length. We also assumed a maximum wing rotation at 60°. For data sources, see [19], [33], [34], and [35].

TABLE III
NONDIMENSIONAL STABILITY DERIVATIVES

Species	X_u^+	Y_v^+	Z_w^+	L_p^+	L_v^+	M_q^+	M_u^+	N_r^+
Fruit fly (*Drosophila melanogaster*)	-1.48	-1.39	-1.58	-0.56	0.87	-0.19	-0.92	-1.36
Hawkmoth (*Manduca sexta*)	-1.97	-0.78	-1.51	-0.81	0.45	-0.13	-1.13	-1.71
Stalk-eyed fly (*Cyrtodiopsis dalmanni*)	-1.52	-1.43	-1.62	-0.89	2.37	-0.31	-2.52	-2.17
Bumblebee (*Bombus*)	-1.79	-1.05	-1.56	-0.81	1.03	-0.19	-1.74	-1.81

TABLE IV
DIMENSIONAL AND NONDIMENSIONAL EIGENVALUES

Species		Longitudinal			Lateral		
		Mode 1	Mode 2	Mode 3	Mode 4	Mode 5	Mode 6
Fruit fly (*Drosophila melanogaster*)	λ_i	-39.15	14.17 ± 30.62i	-5.11	-143.02	9.12 ± 34.85i	-43.30
	λ_i^+	-0.18	0.067 ± 0.14 i	-0.024	-0.67	0.043 ± 0.16i	-0.20
Hawkmoth (*Manduca sexta*)	λ_i	-13.66	4.49 ± 10.37i	-2.24	-27.42	1.15 ± 6.95i	-15.16
	λ_i^+	-0.53	0.17 ± 0.40i	-0.09	-1.05	0.04 ± 0.27i	-0.58
Stalk-eyed fly (*Cyrtodiopsis dalmanni*)	λ_i	-22.20	9.10 ± 18.03i	-2.66	-53.24	7.87 ±18.82i	-21.14
	λ_i^+	-0.13	0.05 ± 0.11i	-0.02	-0.31	0.05 ± 0.11i	-0.12
Bumblebee (*Bombus*)	λ_i	-23.11	8.56 ±18.20i	-2.59	-55.37	4.01 ±12.79i	-15.59
	λ_i^+	-0.15	0.06 ± 0.12i	-0.02	-0.36	0.03 ± 0.08i	-0.10

Subscript, i.e., i = 1--6, denotes the number of modes. Modes 1, 2, 3 and modes 4, 5, 6 are associated with longitudinal and lateral dynamics separately. Eigenvalues (dimension of hertz) are nondimensionalized by dividing the flapping frequency n. The inverse of Re(λ_i) and Re(λ_i^+) indicate the dimensional and nondimensional time constants of the corresponding mode, where Re() denotes the real part of a complex number.

TABLE V
NONDIMENSIONAL EIGENVECTORS FOR DECOUPLED LONGITUDINAL AND LATERAL DYNAMICS

Species	Disturbed state variables	Longitudinal Mode 1	Longitudinal Mode 2	Longitudinal Mode 3	Disturbed state variables	Lateral Mode 4	Lateral Mode 5	Lateral Mode 6
Fruit fly (*Drosophila melanogaster*)	δu^+	0.21 (180°)	0.20 (-58°)	0	δv^+	0.05 (0°)	0.19 (111°)	0.19 (0°)
	δw^+	0	0	1 (0°)	δp^+	0.67 (180°)	0.17 (75°)	0.20 (180°)
	δq^+	0.19 (180°)	0.16 (65°)	0	δr^+	0.83 (0°)	0.04 (-53°)	0.20 (180°)
	$\delta\theta_b$	1 (0)	1(0°)	0	$\delta\phi_b$	1 (0°)	1 (0°)	1 (0°)
Hawkmoth (*Manduca sexta*)	δu^+	0.41 (180°)	0.35 (-54°)	0	δv^+	0.17 (0°)	0.56 (108°)	0.32 (0°)
	δw^+	0	0	1 (0°)	δp^+	1.05 (180°)	0.29 (81°)	0.58 (180°)
	δq^+	0.53 (180°)	0.43 (67°)	0	δr^+	4.24 (0°)	0.01 (-33°)	0.11 (180°)
	$\delta\theta_b$	1 (0°)	1 (0°)	0	$\delta\phi_b$	1 (0°)	1 (0°)	1 (0°)
Stalk-eyed fly (*Cyrtodiopsis dalmanni*)	δu^+	0.22 (180°)	0.20 (-57°)	0	δv^+	0.08 (0°)	0.20 (118°)	0.23 (0°)
	δw^+	0	0	1 (0°)	δp^+	0.31 (180°)	0.12 (67°)	0.12 (180°)
	δq^+	0.13 (180°)	0.12 (63°)	0	δr^+	0.92 (0°)	0.05 (-68°)	0.15 (180°)
	$\delta\theta_b$	1 (0°)	1 (0°)	0	$\delta\phi_b$	1 (0°)	1 (0°)	1 (0°)
Bumblebee (*Bombus*)	δu^+	0.11 (180°)	0.10 (-57°)	0	δv^+	0.04 (0°)	0.15 (114°)	0.16 (0°)
	δw^+	0	0	1 (0°)	δp^+	0.36(180°)	0.09 (73°)	0.10 (180°)
	δq^+	0.15 (180°)	0.13 (65°)	0	δr^+	0.65 (0°)	0.03 (-55°)	0.09 (180°)
	$\delta\theta_b$	1 (0°)	1 (0°)	0	$\delta\phi_b$	1 (0°)	1 (0°)	1 (0°)

Nondimensional eigenvectors are expressed in their magnitudes and phase angles (in parentheses), and normalized to give the pitch angle $\delta\theta_b$ (or the roll angle ϕ_b) a magnitude of 1 rad and phase angle of zero (except Modes 3 and 6). δu, δv, and δw are nondimensionalized by $2\Phi nR\hat{r}_2$, and δp, δq, and δr are nondimensionalized by n.

REFERENCES

[1] R. Dudley, *The Biomechanics of Insect Flight*. Princeton, NJ: Princeton Univ. Press, 2000.

[2] S. N. Fry, R. Sayaman, and M. H. Dickinson, "The aerodynamics of free-flight maneuvers in Drosophila," *Science*, vol. 300, pp. 495–498, Apr. 2003.

[3] S. P. Sane, "The aerodynamics of insect flight," *J. Exp. Biol.*, vol. 206, pp. 4191–4208, Dec. 2003.

[4] J. M. Birch and M. H. Dickinson, "Spanwise flow and the attachment of the leading-edge vortex on insect wings," *Nature*, vol. 412, pp. 729–733, 2001.

[5] J. M. Birch, W. B. Dickson, and M. H. Dickinson, "Force production and flow structure of the leading edge vortex on flapping wings at high and low Reynolds numbers," *J. Exp. Biol.*, vol. 207, pp. 1063–1072, Mar. 2004.

[6] M. H. Dickinson, F. O. Lehmann, and S. P. Sane, "Wing rotation and the aerodynamic basis of insect flight," *Science*, vol. 284, pp. 1954–1960, Jun. 1999.

[7] F.-O. Lehmann, "When wings touch wakes: Understanding locomotor force control by wake wing interference in insect wings," *J. Exp. Biol.*, vol. 211, pp. 224–233, Jan. 2008.

[8] D. Lentink and M. H. Dickinson, "Rotational accelerations stabilize leading edge vortices on revolving fly wings," *J. Exp. Biol.*, vol. 212, pp. 2705–2719, Aug. 2009.

[9] S. P. Sane and M. H. Dickinson, "The control of flight force by a flapping wing: Lift and drag production," *J. Exp. Biol.*, vol. 204, pp. 2607–2626, Oct. 2001.

[10] S. P. Sane and M. H. Dickinson, "The aerodynamic effects of wing rotation and a revised quasi-steady model of flapping flight," *J. Exp. Biol.*, vol. 205, pp. 1087–1096, Apr. 2002.

[11] Z. J. Wang, "Two-dimensional mechanism for insect hovering," *Phys. Rev. Lett.*, vol. 85, pp. 2216–2219, 2000.

[12] H. Liu, "Integrated modeling of insect flight: From morphology, kinematics to aerodynamics," *J. Comput. Phys.*, vol. 228, pp. 439–459, 2009.

[13] H. Dong, R. Mittal, and F. M. Najjar, "Wake topology and hydrodynamic performance of low-aspect-ratio flapping foils," *J. Fluid Mech.*, vol. 566, pp. 309–343, 2006.

[14] L. Ristroph, G. J. Berman, A. J. Bergou, Z. J. Wang, and I. Cohen, "Automated hull reconstruction motion tracking (HRMT) applied to sideways maneuvers of free-flying insects," *J. Exp. Biol.*, vol. 212, pp. 1324–1335, May 2009.

[15] M. Sun and Y. Xiong, "Dynamic flight stability of a hovering bumblebee," *J. Exp. Biol.*, vol. 208, pp. 447–459, Feb. 2005.

[16] Y. Zhang and M. Sun, "Dynamic flight stability of a hovering model insect: Lateral motion," *Acta Mechan. Sinica*, vol. 26, pp. 175–190, 2009.

[17] M. H. Dickinson, "The initiation and control of rapid flight maneuvers in fruit flies," *Integ. Comp. Biol.*, vol. 45, pp. 274–281, Apr. 2005.

[18] B. Cheng, S. Fry, Q. Huang, and X. Deng, "Aerodynamic damping during rapid flight maneuvers in the fruit fly Drosophila," *J. Exp. Biol.*, vol. 213, pp. 602–612, 2009.

[19] T. L. Hedrick, B. Cheng, and X. Deng, "Wingbeat time and the scaling of passive rotational damping in flapping flight," *Science*, vol. 324, pp. 252–255, Apr. 2009.

[20] C. T. David, "The relationship between body angle and flight speed in free-flying Drosophila," *Physiol. Entomol*, vol. 3, pp. 191–195, 1978.

[21] H. Buelthoff, T. Poggio, and C. Wehrhahn, "3-D Analysis of the flight trajectories of flies (*Drosophila rnelanogaster*)," *Z. Naturforsch*, vol. 35c, pp. 811–815, 1980.

[22] W. B. Dickson and M. H. Dickinson, "The effect of advance ratio on the aerodynamics of revolving wings," *J. Exp. Biol.*, vol. 207, pp. 4269–4281, Nov. 2004.

[23] B. Cheng, S. N. Fry, Q. Huang, W. B. Dickson, M. H. Dickinson, and X. Deng, "Turning dynamics and passive damping in flapping flight," in *Proc. IEEE Int. Conf. Robot. Autom.*, Kobe, Japan, 2009, pp. 1889–1896.

[24] B. Etkin and L. D. Reid, *Dynamics of Flight: Stability and Control*. New York: Wiley, 1996.

[25] G. K. Taylor and A. L. R. Thomas, "Dynamic flight stability in the desert locust *Schistocerca gregaria*," *J. Exp. Biol.*, vol. 206, pp. 2803–2829, Aug. 2003.

[26] X. Deng, L. Schenato, and S. S. Sastry, "Hovering flight control for a micromechanical flying insect," in *Proc. 40th IEEE Int. Conf. Decision Control*, 2001, pp. 235–241.

[27] R. M. Murray, Z. Li, and S. S. Sastry, *A Mathematical Introduction to Robotic Manipulation*. Boca Raton, FL: CRC, 1994.

[28] R. W. Prouty, *Helicopter Performance, Stability, and Control*. Boston, MA: PWS, 1986.

[29] B. Cheng and X. Deng, "Mathematical modeling of near-hover insect flight dynamics," presented at 2010 ASME Dyn. Syst. Control Conf., Cambridge, MA.

[30] B. Cheng and X. Deng, "Near-hover dynamics and attitude stabilization of an insect model," in *Proc. Amer. Control Conf.*, Baltimore, MD, 2010, pp. 39–44.

[31] P. Perry, B. Cheng, Z. Hu, and X. Deng, "Translational damping on flapping cicada wings," in *Proc. IEEE/RSJ Int. Conf. Intell. Robots and Syst.*, San Francisco, CA, 2011, to be published.

[32] C. P. Ellington, "The aerodynamics of hovering insect flight—Part 3: Kinematics," *Phil. Trans. R. Soc. Lond. B, Biol. Sci.*, vol. 305, pp. 41–78, 1984.
[33] C. P. Ellington, "The aerodynamics of hovering insect flight—Part 2: Morphological parameters," *Phil. Trans. R. Soc. Lond. B, Biol. Sci.*, vol. 305, pp. 17–40, 1984.
[34] G. Ribak and J. G. Swallow, "Free flight maneuvers of stalk-eyed flies: Do eye-stalks affect aerial turning behavior?" *J. Comp. Physiol. A, Neuroethol. Sensory Neural Behav. Physiol.*, vol. 193, pp. 1065–1079, Oct. 2007.
[35] R. Dudley and C. P. Ellington, "Mechanics of forward flight in bumblebees—Part I. Kinematics and morphology," *J. Exp. Biol.*, vol. 148, pp. 19–52, Jan. 1990.

Bo Cheng received the B.S. degree in automation from Zhejiang University, Hangzhou, China, in 2006 and the M.S. degree in mechanical engineering from the University of Delaware, Newark, in 2009. He is currently working toward the Ph.D. degree with the School of Mechanical Engineering, Purdue University, West Lafayette, IN.

His research interests include aerodynamics, modeling of dynamics and control in flapping-wing flight, and the design of biomimetic micro air vehicles.

Xinyan Deng received the B.S. degree in automation from Tianjin University, Tianjin, China, in 1995 and the Ph.D. degree in mechanical engineering from the University of California, Berkeley, in 2004.

She is currently an Assistant Professor with the School of Mechanical Engineering, Purdue University, West Lafayette, IN. Prior to joining Purdue University, she was an Assistant Professor with the Department of Mechanical Engineering, the University of Delaware, Newark, from 2004 to 2009. Her current research interests include bio-inspired robots, micro air vehicles, and underwater vehicles.